Acta Oceanol. Sin., 2019, Vol. 38, No. 5, P. 21–31
https://doi.org/10.1007/s13131-019-1438-y
http://www.hyxb.org.cn
E-mail: hyxbe@263.net

Wave parameters retrieval for dual-polarization C-band synthetic aperture radar using a theoretical-based algorithm under cyclonic conditions

Yingying Ding[1], Juncheng Zuo[1], Weizeng Shao[1*], Jian Shi[2], Xinzhe Yuan[3], Jian Sun[4], Jiachen Hu[1], Xiaofeng Li[5]

[1] Marine Science and Technology College, Zhejiang Ocean University, Zhoushan 316000, China

[2] College of Meteorology and Oceanography, National University of Defense Technology, Nanjing 210007, China

[3] National Satellite Ocean Application Service, Ministry of Natural Resources, Beijing 100081, China

[4] Physical Oceanography Laboratory, Ocean University of China, Qingdao 266100, China

[5] Global Science and Technology, National Oceanic and Atmospheric Administration (NOAA) National Environmental Satellite, Data, and Information Service (NESDIS), College Park, MD 20740, USA

Received 20 February 2019; accepted 11 March 2019

Abstract

Theoretical-based ocean wave retrieval algorithms are applied by inverting a synthetic aperture radar (SAR) intensity spectrum into a wave spectrum, that has been developed based on a SAR wave mapping mechanism. In our previous studies, it was shown that the wave retrieval algorithm, named the parameterized first-guess spectrum method (PFSM), works for C-band and X-band SAR at low to moderate sea states. In this work, we investigate the performance of the PFSM algorithm when it is applied for dual-polarization c-band sentinel-1 (S-1) SAR acquired in extra wide-swath (EW) and interferometric wide-swath (IW) mode under cyclonic conditions. Strong winds are retrieved from six vertical-horizontal (VH) polarization S-1 SAR images using the c-band cross-polarization coupled-parameters ocean (C-3PO) model and then wave parameters are obtained from the image at the vertical-vertical (VV) polarization channel. significant wave height (SWH) and mean wave period (MWP) are compared with simulations from the WAVEWATCH-III (WW3) model. The validation shows a 0.69 m root mean square error (RMSE) of SWH with a –0.01 m bias and a 0.62 s RMSE of MWP with a –0.17 s bias. Although the PFSM algorithm relies on a good quality SAR spectrum, this study confirms the applicability for wave retrieval from an S-1 SAR image. Moreover, it is found that the retrieved results have less accuracy on the right sector of cyclone eyes where swell directly affects strong wind-sea, while the PFSM algorithm works well on the left and rear sectors of cyclone eyes where the interaction of wind-sea and swell is relatively poor.

Key words: wave parameters, synthetic aperture radar, cyclonic condition

Citation: Ding Yingying, Zuo Juncheng, Shao Weizeng, Shi Jian, Yuan Xinzhe, Sun Jian, Hu Jiachen, Li Xiaofeng. 2019. Wave parameters retrieval for dual-polarization C-band synthetic aperture radar using a theoretical-based algorithm under cyclonic conditions. Acta Oceanologica Sinica, 38(5): 21–31, doi: 10.1007/s13131-019-1438-y

1 Introduction

Ocean waves are the main feature of the upper ocean dynamic processes and play an important role in atmosphere-ocean interactions. Moreover, an extreme wave is also a natural hazard in coastal waters. Therefore, waves are a crucial factor in oceanography and offshore engineering. At present, waves are derived from operational wave models and are usually forced by forecast winds. However, forecast waves have less accuracy when using less accurate values for winds. Satellites carrying an altimeter sensor are a remote-sensing technique for wave monitoring over global seas. For instance, open-access wave data derived from such satellites as Topex/Poseidon, Jason-2 and HY-2, have been popularly used by investigators world-wide. The spatial coverage of an altimeter wave is relatively small (~10 km) with a revisit frequency of 10–15 d and the available wave data from an altimeter only covers the track footprints of a satellite orbit. This kind of limitation does not satisfy the requirements of marine research, especially when researching cyclonic conditions. Synthetic aperture radar (SAR) has the capability of monitoring the sea surface with a large swath coverage (up to 600 km) and fine spatial resolution (up to 1 m). SAR-derived waves can improve wave forecasts and make up the gaps in remotely sensed measurements at coastal waters.

Traditionally, the methodology of a wave retrieval algorithm was exploited for deriving a wave spectrum from a SAR intensity spectrum based on the SAR wave mapping mechanism, e.g., tilt modulation, hydrodynamic modulation (Alpers et al., 1981), and non-linear velocity bunching (Alpers and Bruening, 1986). To date, these algorithms have included the "max-planck institute" (MPI) algorithm (Hasselmann and Hasselmann, 1991), the semi

Foundation item: The National Key Research and Development Program of China under contract No. 2017YFA0604901; the National Natural Science Foundation of China under contract Nos 41806005 and 41776183; the Public Welfare Technical Applied Research Project of Zhejiang Province of China under contract No. LGF19D060003.
*Corresponding author, E-mail: shaoweizeng@zjou.edu.cn

parametric retrieval algorithm (SPRA) (Mastenbroek and de Valk, 2000), the partition rescaling and shift algorithm (PARSA) (Schulz-Stellenfleth et al., 2005), and the parameterized first-guess spectrum method (PFSM) (He, 1999; Sun and Guan, 2006). In particular, it has been shown that the PFSM algorithm works for C-band (Lin et al., 2017) and X-band (Shao et al., 2015) SAR at low to moderate sea states. It is necessary to understand that prior information on wind is needed in order to produce a first-guess wave spectrum when applying the theoretical-based algorithms that are used to deal with the modulation transfer function (MTF) of non-linear velocity bunching. Moreover, the MTF of velocity bunching was theoretically derived at low to moderate sea state (Hasselmann and Hasselmann, 1991), therefore, the applicability MTF of velocity bunching at high sea seta needs to be studied. In practice, wind can be directly retrieved from a SAR image.

The geophysical model function (GMF) is commonly applied for wind retrieval from a SAR image. It describes the empirical relationship between a SAR-measured backscattering signal in co-polarization (vertical-vertical (VV) and horizontal-horizontal (HH)), called the normalized radar cross section (NRCS), and a wind vector at 10 m height above the sea surface (Masuko et al., 1986). C-band GMFs include CMOD4 (Stoffelen and Anderson, 1997), CMOD-IFR2 developed at the Institut Francais de Recherche pour Exploitation de la MER (IFREMER) (Quilfen et al., 1998), CMOD5N for neutral wind (Hersbach, 2010), C-SARMOD (Mouche and Chapron, 2015), CMOD7 (Stoffelen et al., 2017) and C-SARMOD2 (Lu et al., 2018). The CMOD family has been well studied over the last few decades and has been implemented for various C-band SAR data, e.g., ENVISAT-ASAR (Yang et al., 2011a), RADARSAT-1/2 (R-1/2) (Yang et al., 2011b; Shao et al., 2014) and Sentinel-1A/1B (S-1) (Monaldo et al., 2016) and Gaofen-3 (GF-3) (Shao et al., 2017a, 2019). However, the backscattering signal encounters a saturation problem at strong winds (probably at wind speeds greater than 25 m/s) (Hwang et al., 2010; Voronovich and Zavorotny, 2014; Shao et al., 2017b), indicating these GMFs do not work under these conditions. Under these circumstances, the PFSM algorithm is not applicable for typhoon and hurricane wave retrieval from SAR images.

Several empirical models, e.g., CWAVE_ERS for ERS-1/2 (Schulz-Stellenfleth et al., 2007), CWAVE_ENVI for ENVISAT-ASAR (Li et al., 2011), CWAVE_S1 for S-1 (Stopa and Mouche, 2007) and CSAR_WAVE for GF-3 (Sheng et al., 2018), have also been developed, and are aimed at directly retrieving the wave parameters from SAR images without having to calculate the complex MTF of each modulation. These models work at low to moderate sea states, because data collection taken at high sea states is unavailable in the tuning process. Although two empirical models are preliminarily exploited for wave retrieval in hurricanes and typhoons (Romeiser et al., 2015; Shao et al., 2018a), these have only been tuned through a few images and simulations from a numerical wave model and they need to be refitted for different SAR bands and imaging modes.

Several recent works are devoted to study the characteristic of typhoon/hurricane generated waves on SAR (Mouche et al., 2017; Hwang and Walsh, 2016; Zhang et al., 2018), however, typhoon and hurricane wave monitoring is still a challenge for the SAR research community. Interestingly, strong winds (up to 55 m/s) can be retrieved from cross-polarization (basically vertical-horizontal, VH) NRCS, because cross-polarization NRCS does not saturate as easily as the co-polarization backscattering signal (Hwang and Fois, 2015; Shao et al., 2017a). Recently, a methodology for strong wind retrieval using C-band cross-polarization NRCS was developed for R-2 SAR (Zhang and Perrie, 2012; Shen et al., 2014; Zhang et al., 2017) and GF-3 SAR (Shao et al., 2018c). This issue presents an interesting question and that is whether the MTF of velocity bunching and PFSM algorithm is suitable for wave retrieval at the VV-polarization channel as using a SAR-derived strong wind from an image at the VH-polarization channel under cyclonic conditions.

We organize this paper as follows: S-1 SAR images and other auxiliary data are introduced in Section 2. Section 3 shows the methodologies of cross-polarization strong wind retrieval algorithms, scheme of co-polarization wave retrieval algorithm PFSM and the setup of WW3 model. The validation is presented in Section 4 when comparing the retrieval results with measurements from the simulations of the numeric wave model WAVEWATCH-III (WW3). The discussion is included in Section 5 and the conclusion and summary are given in Section 6.

2 Description of dataset

In total, six S-1 images with visible cyclone eyes acquired in dual-polarization (VV and VH) during the period of August 27 to September 23, 2016 were made available for this study. These images were acquired in extra wide-swath (EW) and interferometric wide-swath (IW) mode with a pixel size of 40 m and 10 m respectively at both azimuth and range directions. The quick-look images of Typhoon Lionrock, Hurricane Lester, Hurricane Gaston, Hurricane Hermine, and Hurricane Karl overlaying the tracks of cyclones are shown in Fig. 1, in which the maximum wind speeds are up to 60 m/s at the several SAR imaging moments.

Although measurements from a satellite altimeter, e.g., Jason-2, are useful for wave analysis (Liu et al., 2016), wave measurements from altimeter Jason-2 passing the six S-1 SAR images were unavailable. Therefore, the WW3 model (the latest version 5.16) in the spirit of the previous WAM model, which was developed by the National Centers for Environmental Prediction (NCEP) of the National Oceanic and Atmospheric Administration (NOAA), was employed to simulate the wave fields during the period of the five cyclones. Since 1979, the European Centre for Medium-Range Weather Forecasts (ECMWF) has released a daily global reanalysis dataset at intervals of six hours, e.g., sea surface wind and wave parameters, which has a fine spatial resolution. We employed ECMWF winds at 0.125° grids as the forcing fields and water depth information is derived from 30 arc-second topography data consisting of the General Bathymetric Chart of the Oceans (GEBCO) from the British Oceanographic Data Centre (BODC). The WW3 model performs simulations of wave fields well (Bi et al., 2015; Zheng et al., 2016; Liu et al., 2017) and the validation of WW3-simulated hurricane waves against National Data Buoy Center (NDBC) buoys of the NOAA was used in our recent study (see Fig. 8 in Shao et al., 2018c). WW3-simulated wave parameters, e.g., significant wave height (SWH) and mean wave period (MWP), are used to study the accuracy of SAR-derived waves under cyclonic conditions.

In this study, we also use independent sources, e.g., polarimetric radiometer WindSAT, in order to validate the SAR-derived wind speed from VH-polarization S-1 SAR images by using a cross-polarization wind retrieval algorithm. WindSAT is a space borne satellite for measuring sea surface winds using a polarimetric radiometer with a swath coverage of more than 350 km following the orbit, and the standard deviation (STD) of wind speed is about 1.4 m/s as validated against the measurements of aircraft (Meissner and Wentz, 2012). Therefore, WindSAT wind

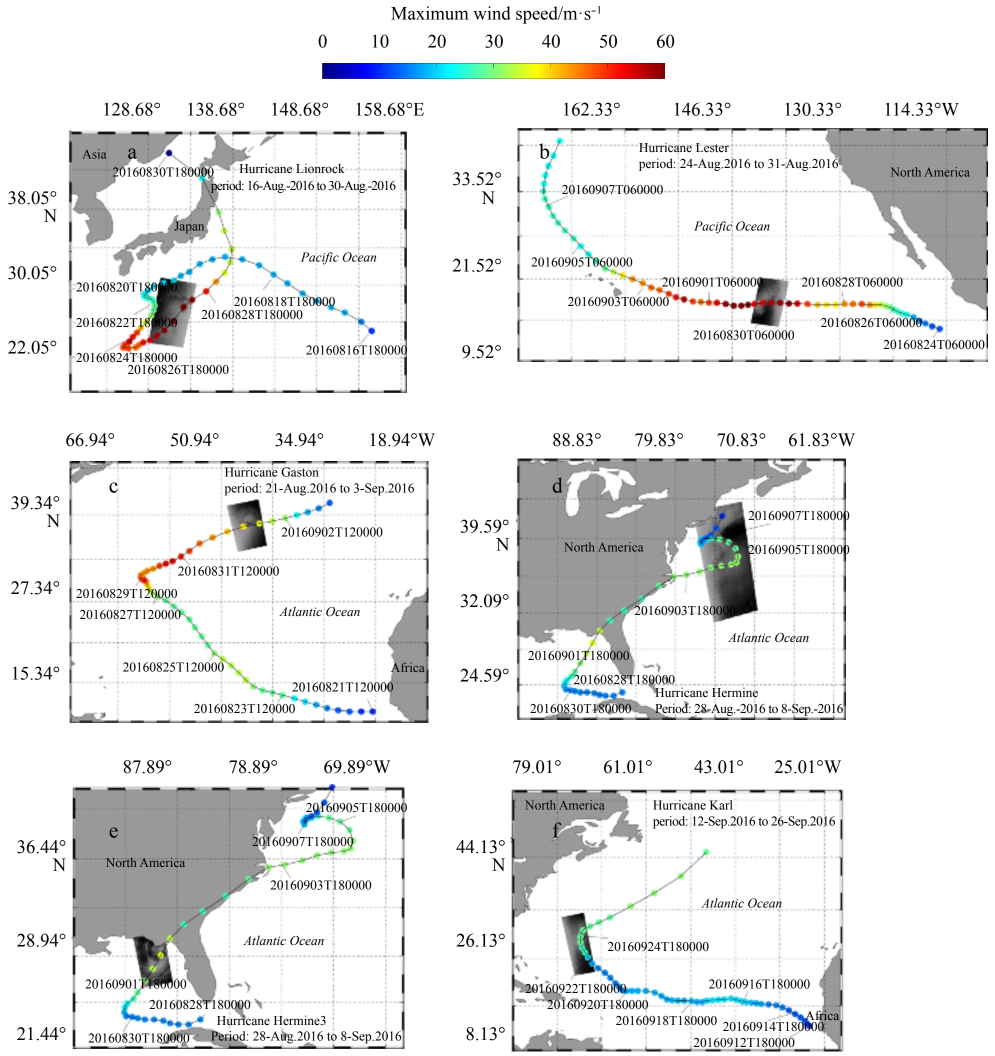

Fig. 1. The quick-look images of six Sentinel-1 (S-1) SAR images in VV-polarization overlaying the tracks of cyclones. a. The image for Typhoon Lionrock acquired in extra wide-swath (EW) mode on August 27, 2016 at 20:53 Universal Time Coordinated (UTC); b. the image for Hurricane Lester acquired in EW mode on August 30, 2016 at 14:46 UTC; c. the image for Hurricane Gaston acquired in EW mode on September 1, 2016 at 20:30 UTC; d. the image for Hurricane Hermine acquired in EW mode on September 4, 2016 at 22:32 UTC; e. the image for Hurricane Hermine acquired in interferometric wide-swath (IW) mode on September 1, 2016 at 23:44 UTC; and f. the image for Hurricane Karl acquired in EW mode on September 23, 2016 at 22:23 UTC.

products satisfy the requirements of global wind monitoring, especially in typhoon and hurricane conditions. It is proved that overall root mean square error (RMSE) difference of the retrieved wind speeds from WindSAT with respect to the H* wind analysis data developed by the Hurricane Research Division (HRD) is 2.75 m/s in hurricanes (Zhang et al., 2016). The WindSAT products with wind speed smaller than 30 m/s are used in this study, due to we think the WindSAT winds are most reliable at such wind condition.

3 Methodology

When applying the PFSM wave retrieval algorithm to retrieve waves, prior information on wind speed is necessary. Therefore, we first present the methodology of the cross-polarization coupled-parameters ocean (C-3PO) model, which was developed for retrieving hurricane winds using cross-polarized SAR NRCS at C-band. Then the theoretically based PFSM wave retrieval algorithm scheme is briefly introduced.

3.1 *C-3PO model*

It was initially revealed in a study by Vachon and Wolfe (2011) that cross-polarization NRCS has a strong linear relationship with wind speed and a quadratic linear model was developed to retrieved wind speed at low to moderate winds (up to 25 m/s). Later, a C-band cross-polarized ocean surface strong wind retrieval model for dual-polarization SAR, named C-2POD, was developed based on a collocated dataset, including R-2 VH-polarized NRCS, measurements from a stepped-frequency microwave radiometer (SFMR) and wind speeds from the NOAA H* wind model (Zhang and Perrie, 2012). In fact, VH-polarized NRCS has also been related to radar incidence angle based on a statistical analysis (Hwang et al., 2015). However, C-2POD models only include the term of wind speed, taking the following function,

$$\sigma_0 = p_1 + p_2 \times U_{10}, \tag{1}$$

where σ_0 is the cross-polarized NRCS united in dB and coefficients p_1 and p_2 are the tuned constants, U_{10} is the wind speed at 10 m above sea surface united in m/s.

As proposed in Zhang et al. (2017), an advanced C-3PO model considers the terms of wind speed and radar incidence angle through theoretical analysis by using a hybrid backscattering model. The C-3PO model is stated as follows:

$$\sigma_0 = A\ (U_{10}) \times [1 + B\ (\theta)], \tag{2a}$$

$$A(U_{10}) = a_1 \times U_{10}^2 + a_2 \times U_{10} + a_3, \tag{2b}$$

$$B(\theta) = b_1 \times \frac{\theta - 34.5}{34.5}, \tag{2c}$$

where σ_0 is the cross-polarized NRCS united in dB, θ is the radar incidence angle united in degree and matrix a and coefficient b_1 are the tuned constants. The C-3PO model has a better performance than the C-2POD model, because a 2.81 m/s RMSE of wind speed is achieved when using the C-3PO model at wind speeds ranging from 9 to 40 m/s, which is less than a 2.90 m/s RMSE using the C-2POD model (Zhang et al., 2017).

3.2 *The PFSM algorithm*

The advantage of the PFSM algorithm is that a SAR-derived wave spectrum is composed of two portions, including wind-sea and swell spectrum, which are retrieved from two corresponding portions separated from a prior SAR spectrum. The separation wave number k_s is calculated using the following equation,

$$k_s = \left(\frac{2.87gV^2}{R^2U_{10}^4\cos^2\varphi\left(\sin^2\varphi\sin^2\theta + \cos^2\varphi\right)} \right)^{0.33}, \tag{3}$$

where g is the gravity acceleration, V is the satellite flight velocity, R is the satellite slant range, U_{10} is the SAR-derived wind speed, θ is the radar incidence angle and φ is the angle of wave propagation direction relative to radar look direction. The portion of the SAR spectrum at wave numbers greater than the separation wave number k_s is non-linearly mapped by the wind-sea and the left portion is linearly mapped by the swell.

For wind-sea retrieval, a "first-guess" spectrum is produced using the widely-used parametric JONSWAP model (see Appendix) after searching for several best-fit parameters of the model, including the sea surface wind speed at 10 m height U_{10}, wave propagation velocity at peak c_p and wave propagation direction at peak φ, which are prior obtained from a SAR image, similar to the SPRA scheme. Following this, the MPI scheme is employed to retrieve the wind-sea spectrum by minimizing a cost function (Hasselmann and Hasselmann, 1991). In the meantime, the swell spectrum is directly obtained by inverting the linear-mapping SAR spectrum, which considers the tilt modulation and hydrodynamic modulation (Alpers et al., 1981) without the velocity bunching (Hasselmann and Hasselmann, 1991). The detailed flowchart of retrieval process has been exhibited as Fig. 2 in our previous study (Shao et al., 2015).

According to traditional wave theory, SWH H_s and MWP T_0 is calculated using Eqs (4) and (5) from a retrieved one-dimensional wave number spectrum W_k,

$$H_s = 4 \times \sqrt{\int W_k \mathrm{d}k}, \tag{4}$$

$$T_0 = \frac{\int W_k \mathrm{d}k}{\int k^2 W_k \mathrm{d}k}. \tag{5}$$

3.3 *WW3 model setup*

As mentioned in Section 2, ECMWF winds at 0.125° grids are the forcing field for the wave simulation. It should be noted that ECMWF winds have a coarser spatial resolution than water depth data from 30 arc-second GEBCO. Therefore, ECMWF winds and GEBCO bathymetric data are both bi-linearly interpolated to be 0.1° in order to obtain reasonable simulations. The simulated two-dimensional wave spectrum is default resolved into 24 regular azimuthal directions at an interval of 15° and the frequency bins f are logarithmically ranged from 0.041 18 to 0.718 6 at an interval of $\Delta f/f$=0.1. The time step of spatial propagation is set to 300 s in both the longitude and latitude directions. In particular, the package of the non-linear term for four wave-wave interactions (quadruplets), named Generalized Multiple Discrete Interaction Approximation (DIA), was implemented for the WW3 model, because it showed a good performance for simulation of typhoon waves according to our recent study (Shao et al., 2018b).

The global simulations from the WW3 model with 0.5° grids are treated as the open boundary. The ultimate WW3-simulated wave fields at 0.2° grids, including the spatial coverages of typhoon and hurricanes, are stored at an interval of 30 min, indicating that the time difference between SAR acquisition time and WW3-simulated results is within 15 min.

4 Validation

In this section, we first present the validation of SAR-derived wind speed against measurements from WindSAT. Then a comparison between the inverted wave parameters and WW3-simulated results is shown.

4.1 *Wind speed*

Figure 2 shows the SAR-derived wind maps corresponding to the six S-1 SAR images acquired in VH-polarization, in which the cyclone eyes are clearly observed. Although the retrieved wind speed is up to 40 m/s, the saturation problem is not found which encounters as applying the C-band co-polarization GMFs. However, discontinuities exist in the retrieved wind maps, indicated by more obvious changes of wind speed at the edge of each radar beam than in other regions. This is caused by the instrumental noise of the radar beam, because the S-1 SAR image acquired in EW and IW mode is comprised of several radar beams. In fact, R-2 (Shen et al., 2014) and GF-3 (Shao et al., 2018c) SAR acquired in dual-polarization also suffer from this problem. For this reason, the European Space Agency (ESA) is privately working on reducing the influence of instrumental noise by means of re-calibrating the S-1 SAR image.

The sub-scenes of S-1 SAR images covering the WindSAT grids are used here. Moreover, the time difference between collected sub-scenes and WindSAT winds is less than 1 h. In total, in this study, around 1 000 matchups are available. Figure 3 gives a visual comparison, showing the SAR-derived wind speeds when using the empirical C-3PO model and WindSAT winds for 2 m/s of wind speed bin, in which the error bars represent the standard deviation of each bin. It is found that the RMSE of wind speed is 2.9 m/s with a 1.1 m/s bias and there is a trend of underestimation at wind speeds greater than 10 m/s. It is not surprising that this performance is worse than the standard error 2 m/s of SAR-derived wind speed for co-polarization, because the in-

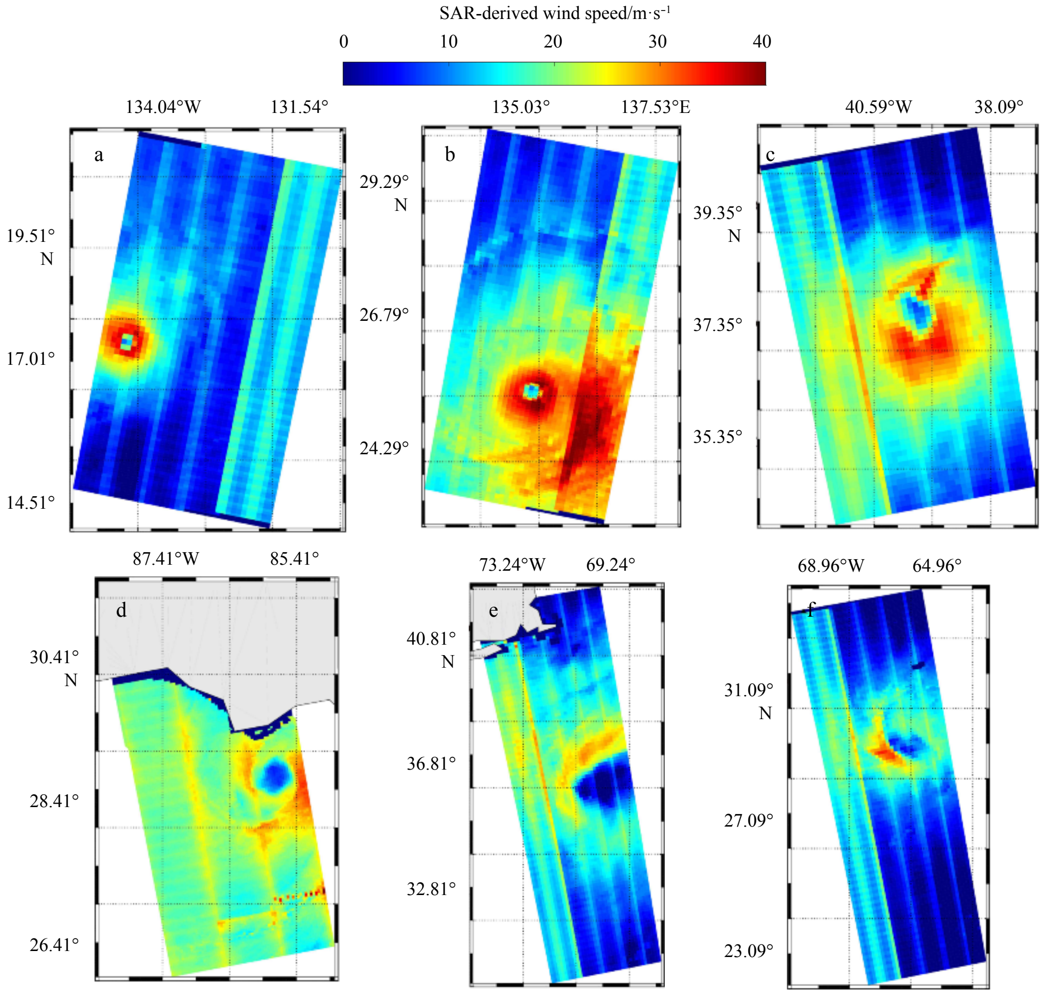

Fig. 2. The SAR-derived wind maps of six S-1 SAR images acquired in VH-polarization. a. The wind map for Typhoon Lionrock on August 27, 2016 at 20:53 UTC; b. the wind map for Hurricane Lester acquired on August 30, 2016 at 14:46 UTC; c. the wind map for Hurricane Gaston on September 1, 2016 at 20:30 UTC; d. the wind map for Hurricane Hermine on September 1, 2016 at 23:44 UTC; e. the wind map for Hurricane Hermine on September 4, 2016 at 22:32 UTC; and f. the wind map for Hurricane Karl on September 23, 2016 at 22:23 UTC.

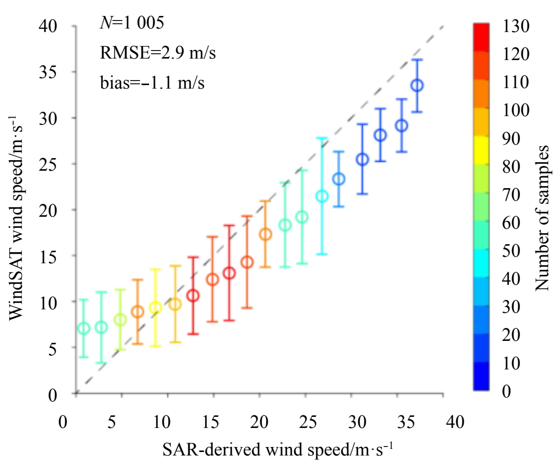

Fig. 3. Comparison between SAR-derived wind speeds using the C-3PO empirical algorithm and WindSAT winds for 2 m/s of wind speed bin, in which the error bars represent the standard deviation of each bin.

strumental noise of the radar beam from S-1 is different from that of the R-2, and the C-3PO model should be adapted for S-1 SAR. However, winds retrieved from VH-polarization SAR images do not encounter the saturation problem. In this situation, we think the retrieved wind is useful for wave retrieval from VV-polarization S-1 SAR images.

4.2 *Wave parameters*

In the wave retrieval process, the whole S-1 SAR image is divided into a number of sub-scenes with 128×128 pixels, which have a spatial coverage of 1×1 km² and 4×4 km² for EW and IW mode, respectively. It is well known that the non-linear effect due to velocity bunching is more pronounced in extreme weather conditions, causing the short waves to be undetectable. Additionally, precipitation also contaminates the SAR backscattering signature of cyclones. In this circumstance, the inhomogeneous sub-scene with poor-quality SAR intensity spectra, where the ratio of image variance and squared image mean is greater than 1.05 (Li et al., 2011), are excluded here. Out of those sub-scenes, φ is extracted from the SAR intensity spectrum, which is an indispensable variable when employing the PFSM algorithm.

As an example, we present the sub-scene extracted from the

S-1 SAR image taken on September 1, 2016 at 23:44 UTC in Hurricane Hermine, as shown in Fig. 4a. Figure 4b shows the two-dimensional SAR spectrum of the corresponding sub-scene in polar coordinates. The retrieved one-dimensional wave spectrum is shown in Fig. 4c. The SAR-derived SWH is 1.8 m and MWP is 5.4 s, while SWH is 2.4 m and MWP is 5.2 s from the WW3 model.

In order to systematically evaluate the retrieval accuracy of SWH and MWP, we compare the retrieval results with simulations from the WW3 model at strong winds. Figure 5 shows that the RMSE of SWH is 0.69 m with a –0.01 m bias and the RMSE of MWP is 0.62 s with a –0.17 s bias when using the PFSM algorithm. It is found that there is larger deviation at low sea state. We think this is caused by inaccurate wind speeds retrieved from VH-polarization S-1 SAR images at low winds smaller than 5 m/s. The accuracy of wave parameters retrieval is anticipated to be improved using more accurate wind speeds from co-polarization S-1 SAR images at low winds or re-calibrating images with low instrumental noise at the edge of radar beams. The pixel size of collected S-1 SAR images are 40 m and 10 m for azimuth and range directions, respectively, indicating that ocean wave with wave length less than 50 m (approximately a 5 s MWP) cannot been measured due to the coarse spatial resolution of collected SAR images. This is the probable explanation that the minimum MWP of retrieved waves is about 5 s in Fig. 5.

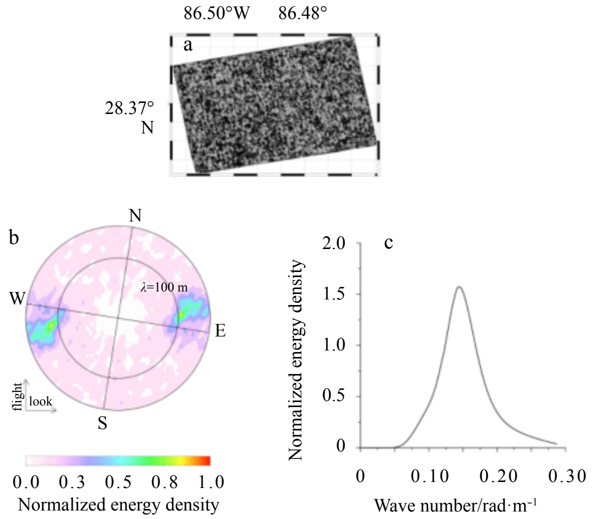

Fig. 4. The retrieval result for a case study. a. The sub-scene extracted from the S-1 SAR image taken on September 1, 2016 at 23:44 UTC in Hurricane Hermine; b. the two-dimensional SAR spectrum, corresponding to Fig. a; and c. one-dimensional wave spectra retrieved using the PFSM algorithm.

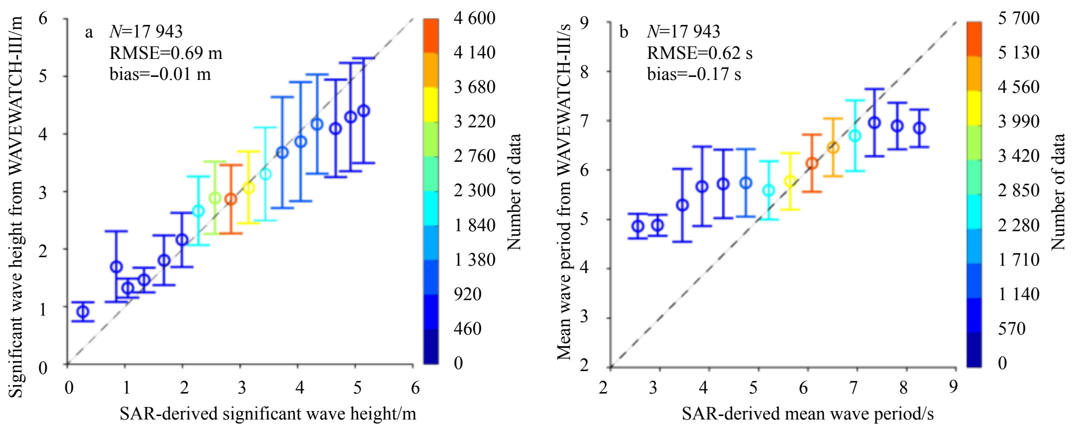

Fig. 5. Comparison between SAR-derived wave parameters using the PFSM algorithm and simulations from WAVEWATCH-III model, in which the error bars represent the standard deviation of each bin. a. Significant wave height for a 0.5 m bin, and b. mean wave period for a 0.5 s bin.

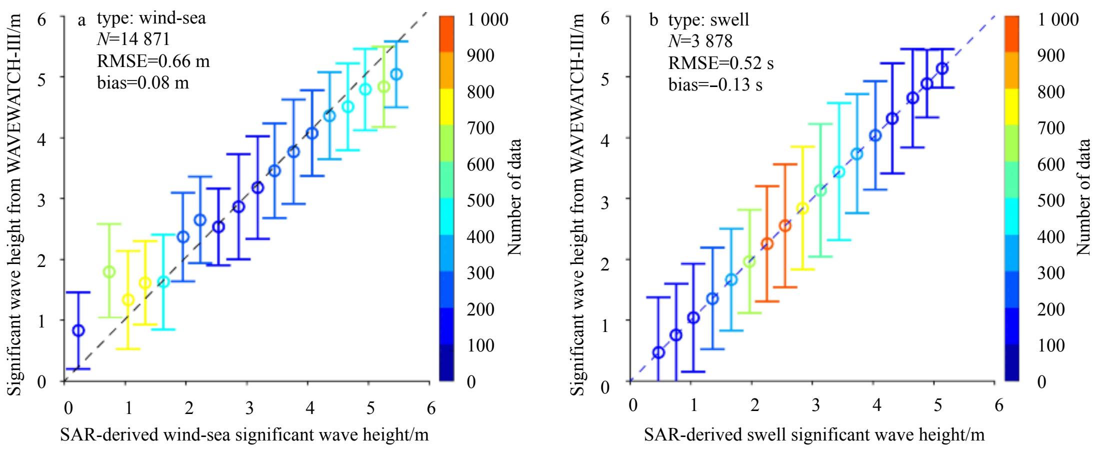

Fig. 6. Comparison between SAR-derived significant wave height using the PFSM algorithm and simulations from WAVEWATCH-III model, in which the error bars represent the standard deviation of each bin. a. Wind-sea for a 0.3 m bin, and b. swell for a 0.3 m bin.

We also compare the SAR-derived SWHs of wind-sea and swell with simulations from WW3 model, as shown in Fig. 6. It is not surprising that a 0.52 RMSE of linear-inverted swell SWH is achieved, which is better than a 0.66 RMSE of nonlinear-inverted wind-sea SWH. In general, the above validation indicates, that the PFSM algorithm can be applied for wave retrieval from a S-1 SAR image under cyclonic conditions, which is similar to wave retrieval from C-band SAR at low to moderate sea states.

5 Discussion

As pointed in our previous study (Shao et al., 2017a), wave characteristics under extreme weather conditions are complicated (Hwang, 2016; Hwang and Fan, 2017; Hwang and Walsh, 2016; Young, 2017), e.g., wind-sea dominates at the right side of a cyclone movement, wind-sea and cross swell mix at the left side of a cyclone movement and opposing swell dominates at the rear side. The wave system in Hurricane Gaston moving north-eastern in the Northern Hemisphere is illustrated in Fig. 7 (reproduce the Fig. 8 in Shao et al., 2017a). Therefore, we have undertaken further study around the accuracy of SWH and MWP at different parts of cyclone eyes.

Figure 8 shows cases at the right side of a cyclone eye, where wind-sea dominates in typical conditions of strong winds on the right-hand sector. Wind-sea and swell propagate in the same direction, causing the interaction of swell and strong wind-sea energy. This leads to a situation whereby the inverted waves using the PFSM algorithm show a large deviation from the WW3-simulated results (a 0.74 m RMSE of SWH and a 0.71 s RMSE of MWP) especially at SWH greater than 3 m. In contrast, wind-sea and swell orthogonally propagate at the left side of the cyclone eye, where the wind-sea energy is independent of swell energy. Retrieval results show a 0.59 m RMSE of SWH and a 0.52 s RMSE of MWP, as shown in Fig. 9, indicating a good agreement with simulations from the WW3 mode. As for wave retrieval at the rear of the cyclone where wind-sea and swell propagate in opposite directions, Fig. 10 shows that the RMSE of SWH is 0.60 m and RMSE of MWP is 0.42 s.

6 Conclusion and summary

In our previous studies, it was shown that the theoretically-based PFSM wave retrieval algorithm worked for C- and X-band SAR at low to moderate conditions. From August to September 2016, several cyclones, e.g., Typhoon Lionrock, Hurricane Lester, Hurricane Gaston, Hurricane Hermine, and Hurricane Karl, were captured by S-1. Therefore, it poses an interesting question as to whether wave can be retrieved from an S-1 SAR image acquired in dual-polarization under cyclonic conditions.

Because the co-polarization backscattering signal encounters saturation problems at strong winds, the winds were retrieved from a VH-polarization S-1 SAR image using the C-3PO model. The RMSE of wind speed is 2.9 m/s with a 1.1 m/s bias as compared with a retrieved wind speed of up to 40 m/s using measurements from WindSAT, although the instrumental noise of S-1 SAR results in obvious changes of wind speed around the edge of radar beams. Together with SAR-derived winds, we demonstrate the applicability of the PFSM algorithm at high sea state. Validation against the simulations from the WW3 model shows a 0.69 m RMSE of SWH with a –0.01 m bias and a 0.62 s RMSE of MWP with a –0.17 s bias. We further investigate the performance at dif-

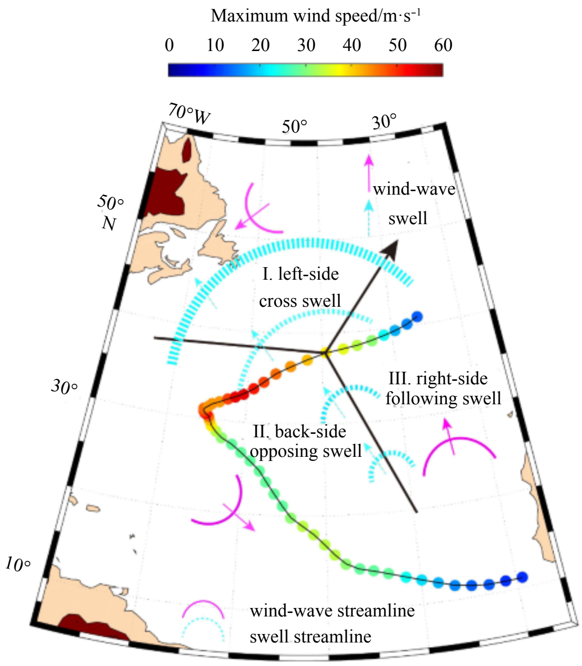

Fig. 7. The wave system in Hurricane Gaston moving north-eastern in the Northern Hemisphere.

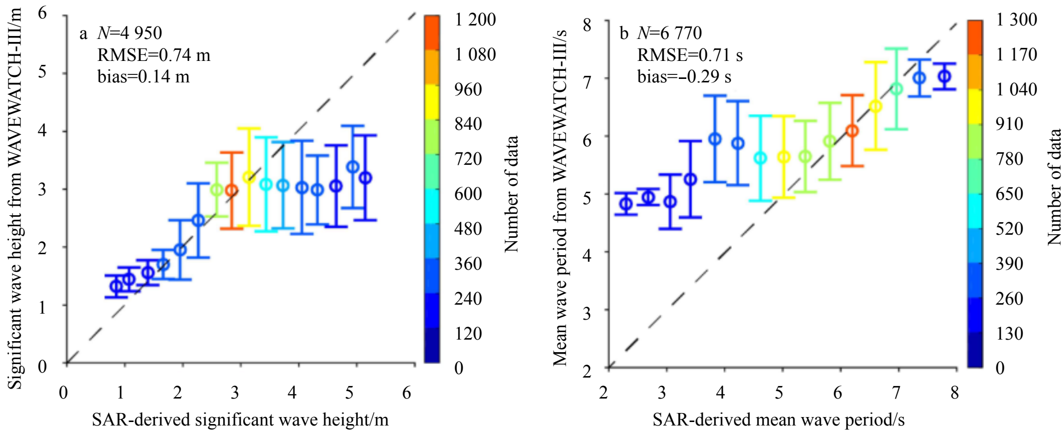

Fig. 8. Comparison between SAR-derived wave parameters using the PFSM algorithm and simulations from WAVEWATCH-III model for cases at the rear of a cyclone eye, in which the error bars represent the standard deviation of each bin. a. Significant wave height for a 0.5 m bin, and b. mean wave period for a 0.5 s bin.

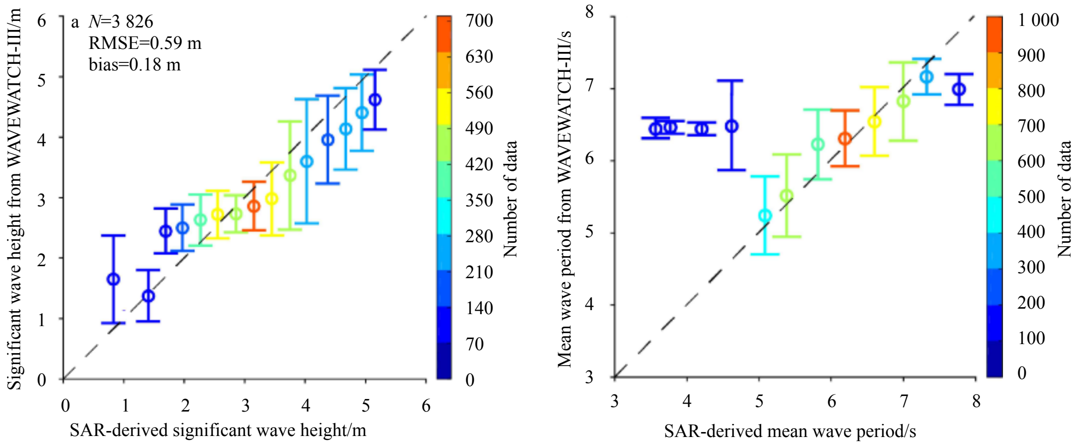

Fig. 9. Comparison between SAR-derived wave parameters using the PFSM algorithm and simulations from WAVEWATCH-III model for cases at the right of a cyclone eye, in which the error bars represent the standard deviation of each bin. a. Significant wave height for a 0.5 m bin and b. mean wave period for a 0.5 s bin.

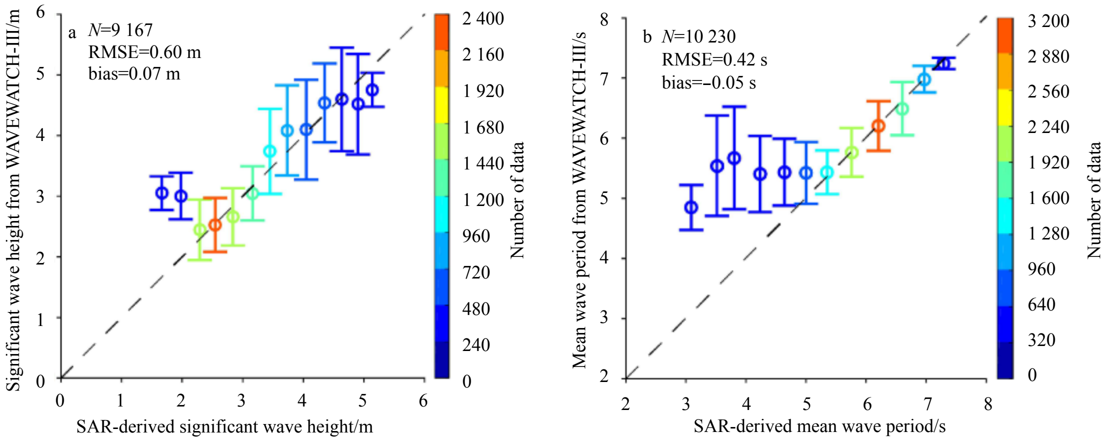

Fig. 10. Comparison between SAR-derived wave parameters using the PFSM algorithm and simulations from WAVEWATCH-III model for cases at the rear of a cyclone eye, in which the error bars represent the standard deviation of each bin. a. Significant wave height for a 0.5 m bin, and b. mean wave period for a 0.5 s bin.

ferent parts of cyclone eyes. The interaction between swell energy and strong wind-sea energy to the right of a cyclone eye leads to less accurate retrieval results than that at left and rear of a cyclone eye, where this type of interaction is relatively poor.

It is concluded that the PFSM algorithm is suitable for estimating wave parameters from a C-band S-1 SAR image under cyclonic conditions, although the PFSM algorithm does rely on a good quality of SAR spectrum. The adaptability of the PFSM algorithm in details will be further studied through more images the improvement of MTF at high winds, e.g., the change of sea water dielectric coefficient and feature of azimuthal cut-off of velocity bunching.

Acknowledgements

We appreciate the provision by the National Centers for Environmental Prediction (NCEP) of National Oceanic and Atmospheric Administration (NOAA) of the source code for the WAVEWATCH-III (WW3) model supplied free of charge. We also thank the following: European Space Agency (ESA) for providing Sentinel-1 (S-1) synthetic aperture radar (SAR) images via https://scihub.copernicus.eu. The European Centre for Medium-Range Weather Forecasts (ECMWF) for providing reanalysis wind data at a 0.125° grid that can be openly downloaded via http://www.ecmwf.int. The General Bathymetry Chart of the Oceans (GEBCO) for data downloaded via: ftp.edcftp.cr.usgs.gov. The information on cyclones provided by NOAA was downloaded via https://coast.noaa.gov/hurricanes. WindSAT winds at a 0.25° grid we kindly provided by the Remote Sensing System (RSS) team, which authorizes an account issued for downloading the data via the sever: ftp.remss.com. The views, opinions, and findings contained in this report are those of the authors and should not be construed as an official NOAA or U.S. Government position, policy or decision.

References

Alpers W R, Bruening C. 1986. On the relative importance of motion-related contributions to the SAR imaging mechanism of ocean surface waves. IEEE Transactions on Geoscience and Remote Sensing, GE-24(6): 873–885, doi: 10.1109/TGRS.1986.289702

Alpers W, Ross D B, Rufenach C L. 1981. On the detectability of ocean surface waves by real and synthetic aperture radar. Journal of Geophysical Research, 86 (C7): 6481–6498

Bi Fan, Song Jinbao, Wu Kejian, et al. 2015. Evaluation of the simulation capability of the Wavewatch III model for Pacific Ocean wave. Acta Oceanologica Sinica, 34(9): 43–57, doi: 10.1007/s13131-015-0737-1

Hasselmann K, Hasselmann S. 1991. On the nonlinear mapping of an ocean wave spectrum into a synthetic aperture radar image spectrum and its inversion. Journal of Geophysical Research: Oceans, 96(C6): 10713–10729, doi: 10.1029/91JC00302

He Yijun. 1999. A parametric method of retrieving ocean wave spectra from synthetic aperture radar images. Chinese Sciences Bulletin, 44(13): 1218–1224, doi: 10.1007/BF02885970

Hersbach H. 2010. Comparison of C-band scatterometer CMOD5.N equivalent neutral winds with ECMWF. Journal of Atmospheric and Oceanic Technology, 27(4): 721–736, doi: 10.1175/2009JTECHO698.1

Hwang P A. 2016. Fetch- and duration-limited nature of surface wave growth inside tropical cyclones: With applications to air–sea exchange and remote sensing. Journal of Physical Oceanography, 46(1): 41–56, doi: 10.1175/JPO-D-15-0173.1

Hwang P A, Fan Yalin. 2017. Effective fetch and duration of tropical cyclone wind fields estimated from simultaneous wind and wave measurements: Surface wave and air–sea exchange computation. Journal of Physical Oceanography, 47(2): 447–470, doi: 10.1175/JPO-D-16-0180.1

Hwang P A, Stoffelen A, van Zadelhoff G J, et al. 2015. Cross-polarization geophysical model function for C-band radar backscattering from the ocean surface and wind speed retrieval. Journal of Geophysical Research: Oceans, 120(2): 893–909 doi: 10.1002/2014JC010439

Hwang P A, Walsh E J. 2016. Azimuthal and radial variation of wind-generated surface waves inside tropical cyclones. Journal of Physical Oceanography, 46(9): 2605–2621, doi: 10.1175/JPO-D-16-0051.1

Hwang P A, Zhang Biao, Toporkov J V, et al. 2010. Comparison of composite Bragg theory and quad-polarization radar backscatter from RADARSAT-2: With applications to wave breaking and high wind retrieval. Journal of Geophysical Research: Oceans, 115(C8): C08019

Li Xiaoming, Lehner S, Bruns T. 2011. Ocean wave integral parameter measurements using Envisat ASAR wave mode data. IEEE Transactions on Geoscience and Remote Sensing, 49(1): 155–174, doi: 10.1109/TGRS.2010.2052364

Lin Bo, Shao Weizeng, Li Xiaofeng, et al. 2017. Development and validation of an ocean wave retrieval algorithm for VV-polarization Sentinel-1 SAR data. Acta Oceanologica Sinica, 36(7): 95–101, doi: 10.1007/s13131-017-1089-9

Liu Qingxiang, Babanin A, Fan Yalin, et al. 2017. Numerical simulations of ocean surface waves under hurricane conditions: assessment of existing model performance. Ocean Modelling, 118: 73–93, doi: 10.1016/j.ocemod.2017.08.005

Liu Qingxiang, Babanin A V, Zieger S, et al. 2016. Wind and wave climate in the Arctic Ocean as observed by altimeters. Journal of Climate, 29(22): 7957–7975, doi: 10.1175/JCLI-D-16-0219.1

Lu Yiru, Zhang Biao, Perrie W, et al. 2018. A C-band geophysical model function for determining coastal wind speed using synthetic aperture radar. IEEE Journal of Selected Topics in Applied Earth Observations and Remote Sensing, 11(7): 2417–2428, doi: 10.1109/JSTARS.2018.2836661

Mastenbroek C, de Valk C F. 2000. A semiparametric algorithm to retrieve ocean wave spectra from synthetic aperture radar. Journal of Geophysical Research: Oceans, 105(C2): 3497–3516, doi: 10.1029/1999JC900282

Masuko H, Okamoto K, Shimada M, et al. 1986. Measurement of microwave backscattering signatures of the ocean surface using X band and K_a band airborne scatterometers. Journal of Geophysical Research: Oceans, 91(C11): 13065–13083, doi: 10.1029/JC091iC11p13065

Meissner T, Wentz F J. 2012. The emissivity of the ocean surface between 6 and 90 GHz over a large range of wind speeds and earth incidence angles. IEEE Transactions on Geoscience and Remote Sensing, 50(8): 3004–3026, doi: 10.1109/TGRS.2011.2179662

Monaldo F, Jackson C, Li Xiaofeng, et al. 2016. Preliminary evaluation of Sentinel-1A wind speed retrievals. IEEE Journal of Selected Topics in Applied Earth Observations and Remote Sensing, 9(6): 2638–2642, doi: 10.1109/JSTARS.2015.2504324

Mouche A, Chapron B. 2015. Global C-band Envisat, RADARSAT-2 and Sentinel-1 SAR measurements in copolarization and cross-polarization. Journal of Geophysical Research: Oceans, 120(11): 7195–7207, doi: 10.1002/2015JC011149

Mouche A A, Chapron B, Zhang Biao, et al. 2017. Combined co- and cross-polarized SAR measurements under extreme wind conditions. IEEE Transactions on Geoscience and Remote Sensing, 55(12): 6746–6755, doi: 10.1109/TGRS.2017.2732508

Quilfen Y, Chapron B, Elfouhaily T, et al. 1998. Observation of tropical cyclones by high-resolution scatterometry. Journal of Geophysical Research: Oceans, 103(C4): 7767–7786, doi: 10.1029/97JC01911

Romeiser R, Graber H C, Caruso M J, et al. 2015. A new approach to ocean wave parameter estimates from C-band ScanSAR images. IEEE Transactions on Geoscience and Remote Sensing, 53(3): 1320–1345, doi: 10.1109/TGRS.2014.2337663

Schulz-Stellenfleth J, König T, Lehner S. 2007. An empirical approach for the retrieval of integral ocean wave parameters from synthetic aperture radar data. Journal of Geophysical Research: Oceans, 112(C3): C03019

Schulz-Stellenfleth J, Lehner S, Hoja D. 2005. A parametric scheme for the retrieval of two-dimensional ocean wave spectra from synthetic aperture radar look cross spectra. Journal of Geophysical Research: Oceans, 101(C5): C05004

Shao Weizeng, Hu Yuyi, Yang Jingsong, et al. 2018a. An empirical algorithm to retrieve significant wave height from Sentinel-1 synthetic aperture radar imagery collected under cyclonic conditions. Remote Sensing, 10(9): 1367, doi: 10.3390/rs10091367

Shao Weizeng, Li Xiaofeng, Hwang P, et al. 2017a. Bridging the gap between cyclone wind and wave by C-band SAR measurements. Journal of Geophysical Research: Oceans, 122(8): 6714–6724, doi: 10.1002/2017JC012908

Shao Weizeng, Li Xiaofeng, Sun Jian. 2015. Ocean wave parameters retrieval from TerraSAR-X images validated against buoy measurements and model results. Remote Sensing, 7(10): 12815–12828

Shao Weizeng, Sheng Yexin, Li Huan, et al. 2018b. Analysis of wave distribution simulated by WAVEWATCH-III model in typhoons passing Beibu Gulf, China. Atmosphere, 9(7): 265, doi: 10.3390/atmos9070265

Shao Weizeng, Sheng Yexin, Sun Jian. 2017b. Preliminary assessment of wind and wave Retrieval from Chinese Gaofen-3 SAR imagery. Sensors, 17(8): 1705, doi: 10.3390/s17081705

Shao Weizeng, Sun Jian, Guan Changlong, et al. 2014. A method for sea surface wind field retrieval from SAR image mode data. Journal of Ocean University of China, 13(2): 198–204, doi: 10.1007/s11802-014-1999-5

Shao Weizeng, Yuan Xinzhe, Sheng Yexin, et al. 2018c. Development of wind speed retrieval from cross-polarization Chinese Gaofen-3 synthetic aperture radar in typhoons. Sensors, 18(2): 412, doi: 10.3390/s18020412

Shao Weizeng, Zhu Shuai, Sun Jian, et al. 2019. Evaluation of wind retrieval from co-polarization Gaofen-3 SAR imagery around China Seas. Journal of Ocean University of China, 18(1): 80–92, doi: 10.1007/s11802-019-3779-8

Shen Hui, Perrie W, He Yijun, et al. 2014. Wind speed retrieval from VH dual-polarization RADARSAT-2 SAR images. IEEE Transactions on Geoscience and Remote Sensing, 52(9): 5820–5826, doi: 10.1109/TGRS.2013.2293143

Sheng Yexin, Shao Weizeng, Zhu Shuai, et al. 2018. Validation of significant wave height retrieval from co-polarization Chinese Gaofen-3 SAR imagery using an improved algorithm. Acta Oceanologica Sinica, 37(6): 1–10, doi: 10.1007/s13131-018-1217-1

Stoffelen A, Anderson D. 1997. Scatterometer data interpretation: Estimation and validation of the transfer function CMOD4. Journal of Geophysical Research: Oceans, 102(C3): 5767–5780, doi:

10.1029/96JC02860
Stoffelen A, Verspeek J A, Vogelzang J, et al. 2017. The CMOD7 geophysical model function for ASCAT and ERS wind retrievals. IEEE Journal of Selected Topics in Applied Earth Observations and Remote Sensing, 10(5): 2123–2134, doi: 10.1109/JSTARS.2017.2681806
Stopa J E, Mouche A. 2017. Significant wave heights from Sentinel–1 SAR: validation and applications. Journal of Geophysical Research: Oceans, 122(3): 1827–1848, doi: 10.1002/2016JC012364
Sun Jian, Guan Changlong. 2006. Parameterized first-guess spectrum method for retrieving directional spectrum of swell-dominated waves and huge waves from SAR images. Chinese Journal of Oceanology and Limnology, 24(1): 12–20, doi: 10.1007/BF02842769
Vachon P W, Wolfe J. 2011. C-Band cross-polarization wind speed retrieval. IEEE Geoscience and Remote Sensing Letters, 8(3): 456–459, doi: 10.1109/LGRS.2010.2085417
Voronovich A G, Zavorotny V U. 2014. Full-polarization modeling of monostatic and bistatic radar scattering from a rough sea surface. IEEE Transactions on Antennas and Propagation, 62(3): 1362–1371, doi: 10.1109/TAP.2013.2295235
Yang Xiaofeng, Li Xiaofeng, Pichel W G, et al. 2011a. Comparison of ocean surface winds from ENVISAT ASAR, MetOp ASCAT scatterometer, buoy measurements, and NOGAPS model. IEEE Transactions on Geoscience and Remote Sensing, 49(12): 4743–4750, doi: 10.1109/TGRS.2011.2159802
Yang Xiaofeng, Li Xiaofeng, Zheng Quanan, et al. 2011b. Comparison of ocean-surface winds retrieved from QuikSCAT scatterometer and Radarsat-1 SAR in offshore waters of the U.S. west coast. IEEE Geoscience and Remote Sensing Letters, 8(1): 163–167, doi: 10.1109/LGRS.2010.2053345
Young I R. 2017. A review of parametric descriptions of tropical cyclone wind-wave generation. Atmosphere, 8(10): 194
Zhang Guosheng, Li Xiaofeng, Perrie W, et al. 2017. A hurricane wind speed retrieval model for C-band RADARSAT-2 cross-polarization ScanSAR images. IEEE Transactions on Geoscience and Remote Sensing, 55(8): 4766–4774, doi: 10.1109/TGRS.2017.2699622
Zhang Lei, Liu Guoqiang, Perrie W, et al. 2018. Typhoon/Hurricane-generated wind waves inferred from SAR imagery. Remote Sensing, 10(10): 1605, doi: 10.3390/rs10101605
Zhang Biao, Perrie W. 2012. Cross-polarized synthetic aperture radar: a new potential measurement technique for hurricanes. Bulletin of the American Meteorological Society, 93(4): 531–541, doi: 10.1175/BAMS-D-11-00001.1
Zhang Lei, Yin Xiaobin, Shi Hanqing, et al. 2016. Hurricane wind speed estimation using WindSat 6 and 10 GHz brightness temperatures. Remote Sensing, 8(9): 721, doi: 10.3390/rs8090721
Zheng Kaiwen, Sun Jian, Guan Changlong, et al. 2016. Analysis of the global swell and wind sea energy distribution using WAVEWATCH III. Advances in Meteorology, 2016: 8419580

Appendix:

The two-dimensional wave spectrum $W_{k,\phi}$ in terms of wave number k and propagation direction ϕ has a relationship with the two-dimensional wave spectrum in terms of wave frequency ω and ϕ,

$$W_{k,\phi} = W_\omega \times G_\phi \times \frac{d\omega}{dk}\,, \tag{A1}$$

in which G_ϕ is the directional function and W_ω is the one-dimensional JONSWAP spectrum taking the following function.

$$W_\omega = \alpha \times \frac{g^2}{\omega^2} \times \exp\left[-1.25 \times \left(\frac{\omega_0}{\omega}\right)^4\right] \times \varGamma, \tag{A2}$$

where

$$\varGamma = \gamma^{\exp\left[-\frac{(\omega-\omega p)^2}{2\sigma^2\omega^2}\right]}, \tag{A3}$$

$$\alpha = 0.006 \times \left(\frac{U_{10}}{c_\mathrm{p}}\right)^{0.55}, \tag{A4}$$

$$\omega^2 = g \times k \times \tanh kd, \tag{A5}$$

$$\omega_\mathrm{p} = \frac{g}{c_\mathrm{p}}\,, \tag{A6}$$

$$\sigma = \begin{cases} 0.07 & \omega \leqslant \omega_\mathrm{p}, \\ 0.09 & \omega > \omega_\mathrm{p}. \end{cases} \tag{A7}$$

where g is the gravity acceleration, γ is the peak-enhancement constant assumed to be 3.3, σ is a peak-width parameter, U_{10} is the sea surface wind speed at 10 m height, d is the water depth and c_p is wave propagation velocity at peak.

G_ϕ is defined as the normalized distribution of wave energy density at all propagation directions, which is stated as follows:

$$G_\phi = 0.5 \times \beta \times \mathrm{sech}^2[\beta \times (\phi - \phi_\mathrm{p})], \tag{A8}$$

where

$$\beta = \begin{cases} 2.61 \times \left(\frac{\omega_\mathrm{p}}{\omega}\right)^{1.3} & 0.56 \leqslant \frac{\omega_\mathrm{p}}{\omega} \leqslant 0.95, \\ 2.28 \times \left(\frac{\omega_\mathrm{p}}{\omega}\right)^{1.3} & 0.95 < \frac{\omega_\mathrm{p}}{\omega} \leqslant 1.6, \\ 1.24 & \text{others} \end{cases} \tag{A9}$$

where ϕ_p is the wave propagation direction at peak.

The one-dimensional spectrum W_k is obtained after integrating $W_{k,\phi}$ over all directions,

$$W_k = \int W_{k,\phi}\,d\phi. \tag{A10}$$